ORCA – Online Research @ Cardiff

Changing atmospheric CO$_2$ concentration was the primary driver of early Cenozoic climate

Eleni Anagnostou[1], Eleanor H. John[2]†, Kirsty M. Edgar[2,3]†, Gavin L. Foster[1], Andy Ridgwell[4,5], Gordon N. Inglis[6,7], Richard D. Pancost[6,7], Daniel J. Lunt[4,5] & Paul N. Pearson[2]

[1]Ocean and Earth Science, National Oceanography Centre Southampton, University of Southampton Waterfront Campus, Southampton SO14 3ZH, UK.

[2]School of Earth and Ocean Sciences, Cardiff University, Park Place, Cardiff CF10 3AT, UK.

[3]School of Earth Sciences, Bristol University, BS8 1RJ, UK.

[4]School of Geographical Sciences, Bristol University, BS8 1SS, UK.

[5]Department of Earth Sciences, University of California, Riverside, California 92521, USA.

[6]Organic Geochemistry Unit, School of Chemistry, University of Bristol, Cantock's Close, Bristol BS8 1TS, UK.

[7]Cabot Institute, University of Bristol, Bristol, BS8 1UJ, UK.

†Present addresses: Earth Sciences and Environment, University of the South Pacific, Fiji (E.H.J.); School of Geography, Earth and Environmental Sciences, University of Birmingham, B15 2TT, UK (K.M.E.).

The Early Eocene Climate Optimum (EECO, which occurred about 51 to 53 million years ago)[1], was the warmest interval of the past 65 million years, with mean annual surface air temperature over ten degrees Celsius warmer than during the pre-industrial period[2–4]. Subsequent global cooling in the middle and late Eocene epoch, especially at high latitudes, eventually led to continental ice sheet development in Antarctica in the early Oligocene epoch (about 33.6 million years ago). However, existing estimates place atmospheric carbon dioxide (CO$_2$) levels during the Eocene at 500–3,000 parts per million[5–7], and in the absence of tighter constraints carbon–climate interactions over this interval remain uncertain. Here we use recent analytical and methodological developments[8–11] to generate a new high-fidelity record of CO$_2$ concentrations using the boron isotope (δ^{11}B) composition of well preserved planktonic foraminifera from the Tanzania Drilling Project, revising previous estimates[6]. Although species-level uncertainties make absolute values difficult to constrain, CO$_2$ concentrations during the EECO were around 1,400 parts per million. The relative decline in

CO_2 concentration through the Eocene is more robustly constrained at about fifty per cent, with a further decline into the Oligocene[12]. Provided the latitudinal dependency of sea surface temperature change for a given climate forcing in the Eocene was similar to that of the late Quaternary period[13], this CO_2 decline was sufficient to drive the well documented high- and low-latitude cooling that occurred through the Eocene[14]. Once the change in global temperature between the pre-industrial period and the Eocene caused by the action of all known slow feedbacks (apart from those associated with the carbon cycle) is removed[2–4], both the EECO and the late Eocene exhibit an equilibrium climate sensitivity relative to the pre-industrial period of 2.1 to 4.6 degrees Celsius per CO_2 doubling (66 per cent confidence), which is similar to the canonical range (1.5 to 4.5 degrees Celsius[15]), indicating that a large fraction of the warmth of the early Eocene greenhouse was driven by increased CO_2 concentrations, and that climate sensitivity was relatively constant throughout this period.

Over the past 540 million years, Earth's climate has oscillated between a globally warm 'greenhouse state' and an 'icehouse state' with substantial continental glaciation[16]. The most recent of these transitions occurred between the warmest time interval of the last 65 million years—the EECO (about 14 ± 3 °C warmer than pre-industrial times[2])—and the rapid growth of ice on Antarctica in the earliest icehouse state of the Oligocene (~33.6 Myr ago[1]). It has been suggested that variations in the concentration of the greenhouse gas CO_2 were responsible for both the overall warmth of the Eocene and the subsequent cooling[17]. Recent studies have documented the importance of CO_2 decline for the final step into the icehouse across the Eocene–Oligocene transition[12,18]. Despite this, the few available CO_2 reconstructions vary markedly between different proxy systems, obscuring relationships with the global cooling trend[1,5,19,20] and therefore preventing a robust test of this hypothesis (Fig. 1). Furthermore, fully coupled climate models require CO_2 concentrations ranging from twice 2× to 16× the pre-industrial value (560–4,480 parts per million (p.p.m.); see, for example, ref. 21) in order to replicate reconstructed early Eocene sea surface temperatures (SSTs) and mean annual air temperatures (MATs). Clearly, to use past warm climate states like the early Eocene to evaluate models and our understanding of the climate system, new and more accurate CO_2 reconstructions are needed.

The use of boron isotopes ($\delta^{11}B$) in marine carbonates is a well understood proxy of seawater pH, allowing for high-fidelity reconstructions of atmospheric CO_2 in locations where surface seawater is in near-equilibrium with the atmosphere regarding CO_2 (see refs 9 and 22). Recently, the isotopic fractionation factor of boron in seawater has been experimentally determined[10], our understanding of the evolution of the ocean carbonate system through time has improved[23,24], and it has become apparent through inter-laboratory comparison studies[8] that a potential bias relating to the foraminiferal B/Ca ratio may exist in earlier studies, suggesting that published Eocene $\delta^{11}B$–CO_2 estimates[6,7] need to be revisited. Here we resolve these issues by measuring the $\delta^{11}B$ of well preserved Eocene planktonic foraminifera from the Kilwa group in Tanzania using multi collector inductively coupled plasma mass spectrometry (MC-ICPMS)[9] and a greater array of species, to resolve the potential for species-specific and depth-habitat-related biases in $\delta^{11}B$ more clearly.

The approach we follow to determine atmospheric CO_2 from foraminiferal calcium carbonate $\delta^{11}B$ ($\delta^{11}B_c$) is detailed in the Methods. We analysed foraminifera from five discrete time slices between 36.9 and 53.2 Myr ago recovered by the Tanzania Drilling Project (Extended Data Fig. 1), and we quantified the oxygen isotopic composition ($\delta^{18}O$) of up to 17 different foraminifera species occupying a range of depth habitats to derive the calcification temperature and hence the relative habitat depth of the taxa[25]. In each case we find a decrease of $\delta^{11}B_c$ with increasing depth, consistent with modern ocean $\delta^{11}B_{borate}$ profiles (Fig. 2) and a clustering of the warmest species with a similar $\delta^{11}B_c$.

By applying species-specific $\delta^{11}B$–pH calibrations, $\delta^{11}B_c$ measurements can be converted to pH reconstructions with depth. However, we lack such calibrations for these extinct taxa. The $\delta^{11}B$ vital effects that are a result of foraminiferal physiology (Methods) appear to be reduced in Eocene foraminifera compared to modern taxa for both shallow symbiont-bearing and deeper non-symbiotic planktonic foraminifera. We therefore calculate pH from $\delta^{11}B_c$ using two different approaches to bracket the probable magnitude of $\delta^{11}B$–pH vital effects: (1) we assume that $\delta^{11}B_c = \delta^{11}B_{borate}$ (hereafter the 'borate' calibration), and (2) we assume that the shallower foraminifera in each time slice has the $\delta^{11}B$–pH calibration of the modern mixed-layer-dwelling foraminifera *Trilobatus sacculifer*[22].

The boron isotopic composition of seawater ($\delta^{11}B_{sw}$) is also required to calculate pH, constrained here by two methods, both based on the observation that the reconstructed pH gradient from shallow to deep for a given $\delta^{11}B_{borate}$ gradient in the water column is a function of $\delta^{11}B_{sw}$ because of the nonlinearity of the $\delta^{11}B$–pH proxy (Extended Data Fig. 2, Methods). If we assume $\delta^{11}B_c = \delta^{11}B_{borate}$ we calculate $\delta^{11}B_{sw}$ to be in the range 38.2–38.7‰. This is slightly increased to 38.6–38.9‰ if we use the $\delta^{11}B$–pH calibration of *T. sacculifer* (Methods).

Given the strong positive relationship between $\delta^{11}B$ and pH, it is evident from our $\delta^{11}B_c$ data alone that surface water pH increased through the Eocene (Fig. 3a). However, having determined both $\delta^{11}B_{sw}$ and calcification temperature, we can generate quantitative estimates of upper-ocean pH, and here we propagated a conservative estimate of the relevant uncertainties using a Monte Carlo approach (Methods). Based on these upper-water-column reconstructions and the borate (or *T. sacculifer)* calibration, we estimate that surface water pH increased from 7.66 ± 0.06 (or 7.59 ± 0.06) at 53.2 Myr ago, to 7.80 ± 0.07 (or 7.76 ± 0.06) by 36.9 Myr ago. By extending our knowledge of species depth habitat and $\delta^{11}B_{sw}$ to the $\delta^{11}B_c$ data set of ref. 12 (Methods), it is apparent that surface-water pH continued to increase in the early Oligocene, reaching 7.88 ± 0.05 (or 7.84 ± 0.05) by ~33 Myr ago. Notably, our Eocene surface-water pH estimates are lower than any others reported in the Cenozoic era, including during the warmth of the middle Miocene and Pliocene: minimum pH values of 7.83 (ref. 22) and 7.99 (ref. 26), respectively.

Ocean pH, like seawater CO_2–that is, $[CO_2]_{aq}$—is largely determined by the ratio of total alkalinity to total dissolved inorganic carbon. Hence, to first order, our pH estimates also indicate that $[CO_2]_{aq}$ declined through the Eocene. Given the oligotrophic setting of our site, this further implies that atmospheric CO_2 declined through the study interval. However, quantitative constraints on early Cenozoic CO_2 evolution require a second carbonate system parameter. Here we assume that the surface seawater saturation state for calcite (Ω_{calc}) at our site remained between 5.5 and 7.5, a conservative range that encompasses geochemical model estimates[27] (Methods; Extended Data Fig. 3). Uncertainty was again fully propagated (details in Methods).

As expected given the raw $\delta^{11}B_c$ values and calculated pH, we find that CO_2 decreased (Fig. 3b) for the borate calibration (or the *T. sacculifer* calibration in Extended Data Fig. 4) from $1,400 \pm 470$ p.p.m. (or $1,900 \pm 600$) p.p.m. during the EECO to ≤ 770 p.p.m. (or 920 p.p.m.) from 40.3 Myr ago onwards, reaching a minimum of 550 ± 190 p.p.m. (or 670 ± 210 p.p.m.) in the early Oligocene. Our new data confirm that CO_2 was most probably $\geq 1,000$ p.p.m. (at a 95% confidence interval) during the EECO, consistent with the recently revised estimates using the sodium carbonate mineral nahcolite[11]. Although our younger time slices are in good agreement with alkenone-based CO_2 reconstructions (Extended Data Fig. 4), our early Eocene CO_2 reconstructions are clearly unprecedented in the Cenozoic. At 5–7× the pre-industrial value, our reconstructed EECO CO_2 value can provide tighter constraints on models than those that have been previously available. Critically, our CO_2 reconstructions are lower than required by a number of coupled ocean–atmosphere climate models to achieve a good match with Eocene temperature data[21].

Using our new CO_2 record, the possible role of CO_2 in driving Eocene cooling can be quantitatively examined. The relative change in climate forcing attributable to CO_2 change ($\Delta F_{CO2\text{-vs.-EECO}}$) through the Eocene can be estimated[28] as:

$$\Delta F_{CO2\text{-vs.-EECO}} = 5.32 \times \ln(C_t/C_{EECO}) + 0.39 \times [\ln(C_t/C_{EECO})]^2 \quad (1)$$

where C_{EECO} is the atmospheric CO_2 concentration at the EECO, and C_t refers to the CO_2 reconstruction at a particular time in the Eocene. The CO_2 forcing based on our reconstructions for the Eocene is well correlated with the contemporaneous proxy-derived sea surface cooling, albeit with considerably larger cooling at high latitudes (Fig. 4a, Extended Data Fig. 5a, $R^2 = 0.8$ at low latitudes and 0.9 at high latitudes).

The apparent latitudinal dependency of SST change for a given change in radiative forcing has recently been determined for the last 520,000 years (520 kyr; ref. 13), using CO_2, ice-sheet albedo (which are slow feedbacks), dust and mean annual insolation as forcing terms[29]. Assuming that this latitudinal dependency for a given forcing (Fig. 4b and Methods)[13] is also appropriate for the Eocene, we can calculate the expected SST change as a result of the climate forcing, ΔF_{CO2} (see equation (1)), for each target time slice in our study, for high latitudes (60° N and 60° S; blue lines on Fig. 4b) and low latitudes (30° N to 30° S, red box on Fig. 4b; see Methods) and compare these to a recent SST compilation[14]. The calculated SST change from our

CO_2 reconstructions is within error of the observed, proxy-derived SST evolution of both high and low latitudes through the Eocene (Fig. 4c, Extended Data Fig. 5c) regardless of which $\delta^{11}B$–pH calibration is used. This supports CO_2 as the principal driver of long-term Eocene cooling, although feedback processes involved in causing the observed polar amplification in Fig. 4a and Extended Data Fig. 5a must also play a vital part in determining its pattern.

Our CO_2 reconstructions also allow us to examine the sensitivity of the Earth's temperature to changes in radiative forcing. This is often discussed in terms of Equilibrium Climate Sensitivity (ECS): the global mean surface temperature change (in degrees Celsius) for a doubling of CO_2 after all those feedbacks that operate on the timescale of about a century have time act (the "fast" feedbacks[29]). The ECS can be calculated for the Eocene using:

$$ECS = \Delta T/\Delta F_{CO2\text{-vs-PI}} \times 3.87 \qquad (2)$$

where ΔT is the global mean surface temperature change compared to the pre-industrial period, corrected for the action of those feedbacks that operate on timescales longer than a century (the "slow" feedbacks[29]) (Fig. 4d, Extended Data Fig. 5d); $\Delta F_{CO2\text{-vs.-PI}}$ is calculated as in equation (1), replacing C_{EECO} with pre-industrial CO_2 (278 p.p.m.) because we are interested in forcing change relative to the pre-industrial period (Fig. 4e, Extended Data Fig. 5e); and 3.87 is the climate forcing of a CO_2 doubling (in units of W m^{-2}), calculated using equation (1).

The global mean surface temperature change for the EECO is thought to be ~14 ± 3 °C warmer than the pre-industrial period, and ~5 °C warmer than the late Eocene (35 Myr ago; refs 2 and 29). Recent climate modelling studies have ascribed 4–6 °C of Eocene warmth to changes in boundary conditions (such as palaeotopography and continental configuration) and the action of the slow climate feedbacks (principally the lack of a continental ice sheet on Antarctica and vegetation change[2–4]). If atmospheric CO_2 concentration were the principal driving mechanism for the relative warmth of the EECO and late Eocene, we would expect the Eocene ECS value to fall within the range reported by the Intergovernmental Panel on Climate Change[15], based on climate modelling and observations of the (palaeo)climate system. However, if other climate feedbacks were important that we have not accounted for in our correction of the 'slow' feedbacks[2–4], or if the forcing is not due to CO_2 alone, then the calculated ECS value would be different from that reported by the IPCC. Full

details of how the uncertainties in these various parameters are propagated can be found in the Methods, but from Fig. 4f and Extended Data Fig. 5f it is clear that the average ECS we calculate for the Eocene lies, for the borate (or *T. sacculifer*) approach in the range 2.6–4.6 °C (or 2.1–3.6 °C) per CO_2 doubling (66% confidence) with maximum probability for the EECO of 3.8 °C (or 3.3 °C). This range (2.1–4.6 °C per CO_2 doubling) is similar to the IPCC range (1.5–4.5 °C at 66% confidence[15]). Therefore, the 65% of early and late Eocene warmth attributed to fast feedbacks[2–4,29] is consistent with Eocene warmth being driven by higher atmospheric CO_2 concentrations. This supports the importance of atmospheric CO_2 variability in determining both the warmth of the early Eocene and the cooling that ultimately led to the establishment of the late Cenozoic icehouse.

1. Zachos, J. C., Dickens, G. R. & Zeebe, R. E. An early Cenozoic perspective on greenhouse warming and carbon-cycle dynamics. *Nature* **451,** 279–283 (2008).

2. Caballero, R. & Huber, M. State-dependent climate sensitivity in past warm climates and its implications for future climate projections. *Proc. Natl Acad. Sci. USA* (2013).

3. Lunt, D. J. *et al.* CO_2-driven ocean circulation changes as an amplifier of Paleocene-Eocene thermal maximum hydrate destabilization. *Geology* **38,** 875–878 (2010).

4. Loptson, C. A., Lunt, D. J. & Francis, J. E. Investigating vegetation-climate feedbacks during the early Eocene. *Clim. Past* **10,** 419–436 (2014).

5. Beerling, D. J. & Royer, D. L. Convergent Cenozoic CO_2 history. *Nature Geosci.* **4,** 418–420 (2011).

6. Pearson, P. N. & Palmer, M. R. Atmospheric carbon dioxide concentrations over the past 60 million years. *Nature* **406,** 695–699 (2000).

7. Pearson, P. N. & Palmer, M. R. Middle Eocene seawater pH and atmospheric carbon dioxide concentrations. *Science* **284,** 1824–1826 (1999).

8. Foster, G. L. *et al.* Interlaboratory comparison of boron isotope analyses of boric acid, seawater and marine $CaCO_3$ by MC-ICPMS and NTIMS. *Chem. Geol.* **358,** 1–14 (2013).

9. Foster, G. L. Seawater pH, pCO_2 and $[CO_3^{2-}]$ variations in the Caribbean Sea over the last 130 kyr: a boron isotope and B/Ca study of planktic foraminifera. *Earth Planet. Sci. Lett.* **271,** 254–266 (2008).

10. Klochko, K. *et al.* Experimental measurement of boron isotope fractionation in seawater. *Earth Planet. Sci. Lett.* **248,** 276–285 (2006).

11. Jagniecki, E. A., Lowenstein, T. K., Jenkins, D. M. & Demicco, R. V. Eocene atmospheric CO_2 from the nahcolite proxy. *Geology* **43,** 1075–1078 (2015).

12. Pearson, P. N., Foster, G. L. & Wade, B. S. Atmospheric carbon dioxide through the Eocene–Oligocene climate transition. *Nature* **461,** 1110–1113 (2009).

13. Rohling, E. J. *et al.* Sea surface and high-latitude temperature sensitivity to radiative forcing of climate over several glacial cycles. *J. Clim.* **25,** 1635–1656 (2012).

14. Inglis, G. N. *et al.* Descent toward the Icehouse: Eocene sea surface cooling inferred from GDGT distributions. *Paleoceanography* **30,** 1000–1020 (2015).

15. Intergovernmental Panel on Climate Change (IPCC) *Climate Change 2013: The Physical Science Basis. Contribution of Working Group I to the Fifth Assessment Report of the Intergovernmental Panel on Climate Change* (eds Stocker, T.F. *et al.*) 1-1535 (2013).

16. Crowell, J. C. & Frakes, L. A. Phanerozoic glaciation and the causes of ice ages. *Am. J. Sci.* **268,** 193–224 (1970).

17. Raymo, M. E. & Ruddiman, W. F. Tectonic forcing of late Cenozoic climate. *Nature* **359,** 117–122 (1992).

18. Pagani, M. *et al.* The role of carbon dioxide during the onset of Antarctic glaciation. *Science* **334,** 1261–1264 (2011).

19. Zhang, Y. G. *et al.* A 40-million-year history of atmospheric CO_2. *Phil. Trans. R. Soc. A* **371,** http://dx.doi.org/10.1098/rsta.2013.0096 (2013).

20.   Franks, P. J. *et al.* New constraints on atmospheric CO_2 concentration for the Phanerozoic. *Geophys. Res. Lett.* **41,** http://dx.doi.org/10.1002/2014gl060457 (2014).

21.   Lunt, D. J. *et al.* Warm climates of the past—a lesson for the future? *Phil. Trans. R. Soc. A* **371,** http://dx.doi.org/10.1098/rsta.2013.0146 (2013).

22.   Foster, G. L., Lear, C. H. & Rae, J. W. B. The evolution of pCO_2, ice volume and climate during the middle Miocene. *Earth Planet. Sci. Lett.* **341–344,** 243–254 (2012).

23.   Hönisch, B. *et al.* The geological record of ocean acidification. *Science* **335,** 1058–1063 (2012).

24.   Demicco, R. V., Lowenstein, T. K. & Hardie, L. A. Atmospheric pCO_2 since 60 Ma from records of seawater pH, calcium, and primary carbonate mineralogy. *Geology* **31,** 793–796 (2003).

25.   John, E. H. *et al.* Warm ocean processes and carbon cycling in the Eocene. *Phil. Trans. R. Soc. A* **371,** http://dx.doi.org/10.1098/rsta.2013.0099 (2013).

26.   Martínez-Boti, M. A. *et al.* Plio-Pleistocene climate sensitivity evaluated using high-resolution CO_2 records. *Nature* **518,** 49–54 (2015).

27.   Ridgwell, A. & Schmidt, D. N. Past constraints on the vulnerability of marine calcifiers to massive carbon dioxide release. *Nature Geosci.* **3,** 196–200 (2010).

28.   Byrne, B. & Goldblatt, C. Radiative forcing at high concentrations of well-mixed greenhouse gases. *Geophys. Res. Lett.* **41,** 152–160 (2014).

29.   PALAEOSENS Project Members Making sense of palaeoclimate sensitivity. *Nature* **491,** 683–691 (2012); erratum **494,** 130 (2013).

30.   Bohaty, S. M., Zachos, J. C., Florindo, F. & Delaney, M. L. Coupled greenhouse warming and deep-sea acidification in the middle Eocene. *Paleoceanography* **24,** PA2207 (2009).

**Supplementary Information** is available in the online version of the paper.

Author Contributions E.A. conducted all boron isotope and trace element analyses, performed calculations, and drafted the manuscript. E.H.J. and K.M.E. prepared foraminifer samples and conducted the stable isotope analysis. P.N.P. led the fieldwork, performed the taxonomy and prepared foraminifer samples. A.R. provided cGENIE model results. P.N.P. and G.L.F. designed the study and all authors discussed the results and contributed to the final text.

Author Information Reprints and permissions information is available at www.nature.com/reprints. The authors declare no competing financial interests. Readers are welcome to comment on the online version of the paper. Correspondence and requests for materials should be addressed to E.A. (e.anagnostou@noc.soton.ac.uk).
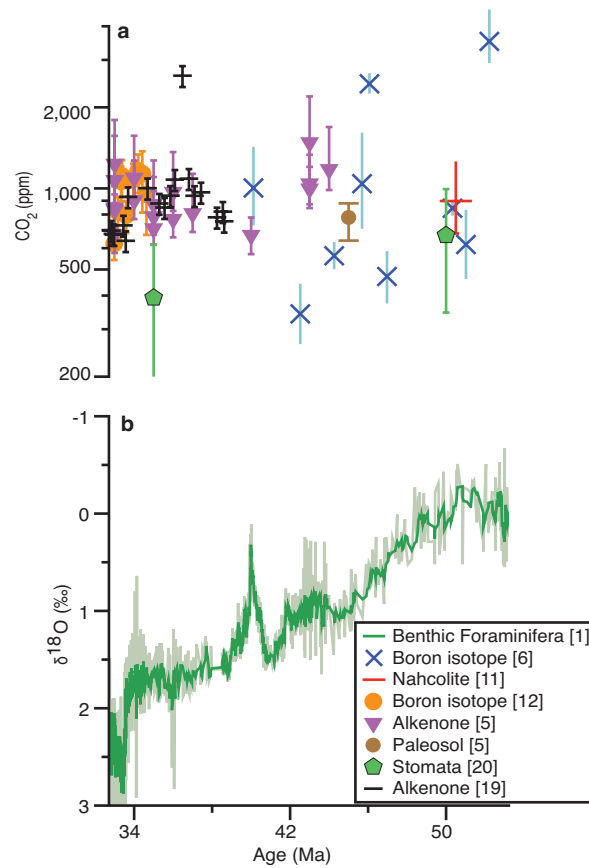
Figure 1 Currently available Eocene atmospheric CO_2 records and benthic foraminiferal $\delta^{18}O$ values. **a**, CO_2 reconstructions[5,6,11,12,19,20] with the 2 s.d. uncertainties. **b**, Benthic foraminiferal $\delta^{18}O$ (ref. 1). The green line shows the five-point moving average of the grey line, with data age modified to account for the revised timing of the MECO[30]. Lower benthic $\delta^{18}O$ values denote warmer bottom-water temperatures (or less ice volume, which is assumed to be minimal in the Eocene). Error bars on $\delta^{18}O$ are smaller than the symbols (Methods).
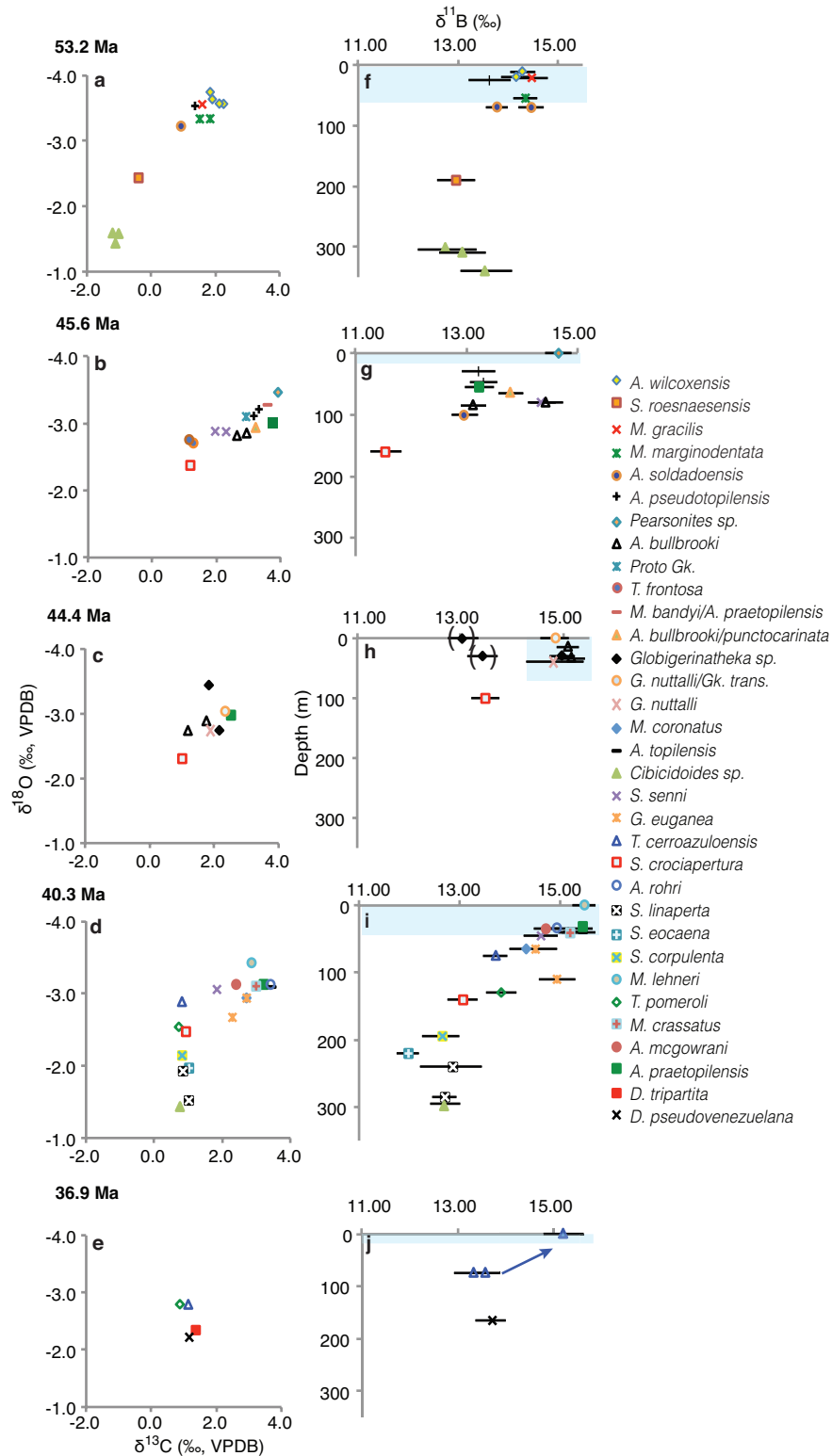
Figure 2 Eocene planktonic foraminiferal multi-species stable isotope arrays. a–e, Foraminiferal δ^13C versus δ^18O for each time slice. **f–j**, Foraminiferal δ^11B values versus δ^18O inferred water depths for each time slice. **h** shows the anomalous behaviour of *Globigerinatheka* spp. (black diamond symbols), in both δ^13C and δ^11B

(see Methods). The blue arrow in **j** shows the correction of *T. cerroazulensis* $\delta^{11}B$ to shallower water values (Methods). Shaded areas in **f** to **j** surround the species used in Fig. 3a. Errors on $\delta^{13}C$ and $\delta^{18}O$ are smaller than symbols. Error bars on $\delta^{11}B$ are 2 s.d. based on long-term precision (Methods). VPDB, the Vienna Pee-Dee belemnite standard. For full species spelling see Supplementary Table 1.
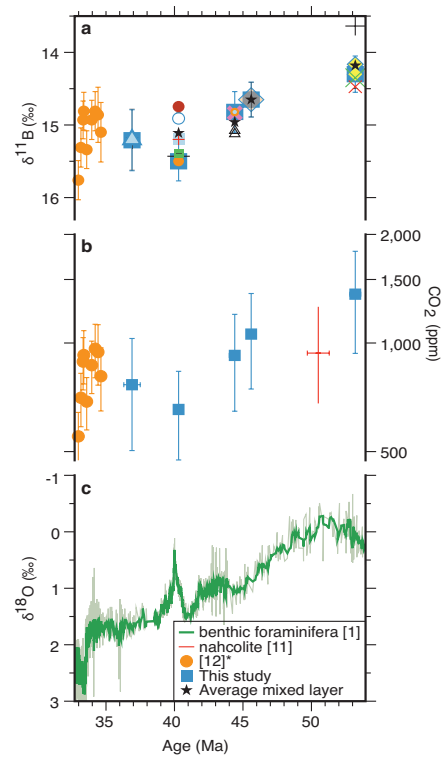
Figure 3 New atmospheric CO_2 reconstructions from shallow planktonic foraminiferal $\delta^{11}B$. a, $\delta^{11}B$ of shallower foraminifera (symbols as in blue-shaded areas of Fig. 2) and asterisks represent the average of those for each timeslice. Blue squares and orange circles represent the warmest species used in **b**. Ref. 12 data are offset (Supplementary Table 2, Methods). **b**, Atmospheric CO_2 assuming $\delta^{11}B_c = \delta^{11}B_{borate}$ using the warmest species of each time slice. Red line is based on ref. 11. **c**, Benthic foraminiferal $\delta^{18}O$ (ref. 1) (as in Fig. 1b). Age error bars (**b**) are based on the ages of the nearest datums, $\delta^{11}B$ errors are as in Fig. 2, and the CO_2 uncertainty is based on the 95% confidence of Monte Carlo error propagation (Methods).
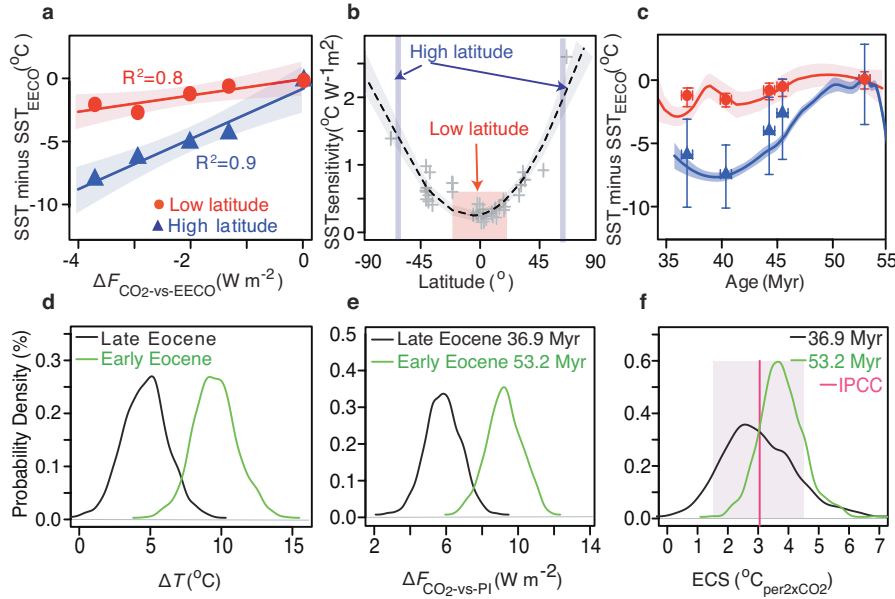
Figure 4 CO₂ as a driver of latitudinal cooling in the Eocene, and ECS analyses of the EECO and late Eocene time slices. a, Evolving relationship between SST[14] for high and low latitudes and the CO_2 forcing of each of our time slices relative to the EECO, with linear regression fits and coefficients of determination (R^2). **b**, Apparent latitudinal SST sensitivity for the last 520 kyr (ref. 13). The dashed line is the second-order polynomial through the SST sensitivity data (grey crosses) of ref. 13. Red shading shows the SST sensitivity estimates averaged as a low-latitude mean, and blue lines show the high-latitude mean. **c**, Reconstructed (lines) and estimated (symbols) SST relative to 53.2 Myr ago. Symbols are estimated using the respective CO_2 reconstructions and the average low-latitude (red circles) and high-latitude (blue triangles) SST sensitivities of **b**. Bold lines show the reconstructed long-term mean SST estimates using the TEX₈₆ proxy[14] at high latitudes (blue >55°) and low latitudes (red <30°) relative to the SST ~53 Myr ago. Error bars represent full propagation of errors at 95% confidence. **d**, Range in mean surface temperature change for early and late Eocene corrected for changes due to slow feedbacks[2,4,21,29]. **e**, Forcing compared to the pre-industrial period calculated using our CO_2 reconstructions for the time slices 53.2 Myr ago (early Eocene) and 36.9 Myr ago (late Eocene). **f**, Probability density functions of ECS for the early and late Eocene compared to IPCC estimates. Shaded bands around lines throughout show 95% confidence intervals.

METHODS

Site information

To obtain optimal records of oxygen, carbon, and boron isotopes, we used well preserved 'glassy' carbonate microfossils from the Palaeogene of the Kilwa Group material drilled by the Tanzanian Drilling Project[31,32]. The core sites were located on the outer shelf or upper continental slope approximately 50–70 km offshore[33], at a palaeolatitude of 19° S, and bathyal palaeowater depths of >300 m (ref. 31). Seismic data, sedimentary facies, nannofossil and planktic foraminiferal assemblages as well as low concentrations of dinoflagellates and a lack of marine biomarkers indicative of high export productivity confirm that these sediments were deposited under open-ocean conditions with waters derived from the Indian Ocean subtropical gyre[34–36], supporting the assumption that $[CO_2]_{aq}$ offshore Tanzania was in (near) equilibrium with the atmosphere with respect to CO_2. This is supported by the "cGENIE" Earth system model estimates with Eocene boundary conditions for offshore Tanzania (Extended Data Fig. 6)[37]; nevertheless, to include the uncertainty of potential disequilibrium with the atmosphere we added ±40 p.p.m. CO_2 uncertainty into our estimates of atmospheric CO_2 using $\delta^{11}B$.

Sample preparation

Approximately 3–4 mg of mono-specific foraminiferal material of a narrow size fraction (for example, ~300 individuals from the 212–250 μm sieve size fraction) were separated from ~10 cm of core material (24 cm for the time slice 53.2 Myr ago) for tandem analyses of all isotopes ($\delta^{18}O$, $\delta^{13}C$ and $\delta^{11}B$) and trace-element composition. Identification of planktonic foraminifera followed ref. 35. Each sample was gently crushed and divided into two parts: one for $\delta^{11}B$ and elemental analyses and another for $\delta^{18}O$ and $\delta^{13}C$ measurements (~100 μg, ~3% per weight). For the timeslices 53.2 Myr ago and 40.3 Myr ago, *Cibicidoides* sp. were also picked for analyses (~1 mg). Splits for elemental and $\delta^{11}B$ analyses were cleaned following established methods[38–40]. Trace-element ratios were determined as in ref. 9 and in all cases Al/Ca ratios were <120 μmol mol^{-1} (typically <100 μmol mol^{-1}), showing efficient foraminiferal cleaning[9,40].

$\delta^{18}O$-$\delta^{13}C$ analyses, temperature reconstructions, relative habitat depth assignments

For all $\delta^{18}O$ and $\delta^{13}C$ analyses, we followed the analytical approach described elsewhere[41], and values are reported relative to the Vienna Pee Dee Belemnite (VPDB) standard, with 1 s.d. standard external precision of ±0.06‰ and ±0.07‰ respectively. All temperature reconstructions are based on the equation of ref. 42, corrected for changes in global ice volume of −0.8‰[43] and palaeolatitude of +0.83‰[44] (following ref. 45). Any further secular trends in seawater $\delta^{18}O$, regional variations in the oxygen isotope ratio of seawater, or differing carbonate ion concentrations are not known with sufficient confidence, so no additional corrections were applied. The lowest $\delta^{18}O$ value in each multi-species depth profile was used to calculate the maximum SST for each time slice with a conservative uncertainty of ±2 °C that encompasses the differences among variable carbonate $\delta^{18}O$ equations (ref. 45), and includes potential uncertainties in $\delta^{18}O_{sw}$ (refs 43 and 46).

Identification of foraminiferal depth habitats is based on $\delta^{18}O$ following refs 25 and 35. This method could carry large uncertainties in the absolute depth reconstructions, but the relative depth habitats of surface and deep taxa are clearly distinguishable from the $\delta^{13}C$ versus $\delta^{18}O$ cross plots (see, for example, refs 25, 45, 47–54), and supported by comparison of $\delta^{11}B$ versus $\delta^{18}O$ profiles (Fig. 2). Further support for our approach is given by the depth assignment of benthic foraminifera *Cibicidoides* based on $\delta^{18}O$ values at 53.2 and 40.3 Myr ago, which at 300–320 m agrees well with the site's palaeowater depth[31]. Any uncertainty in the absolute depth assignment of foraminifera as a result of the 4 °C range (±2 °C) contributes <0.1% uncertainty to the carbonate system calculations and thus is not included, although the temperature uncertainty is fully propagated into our carbonate system estimates (see below).

Boron isotope proxy and analyses
Boron isotopes in planktonic foraminifera residing close to the seawater surface have been used extensively to reconstruct past ocean pH and thus CO_2 concentrations[9,22,55–57]. External reproducibility of $\delta^{11}B_c$ analyses is calculated using the approach of ref. 40 and the relationship of ref. 41.

To reconstruct seawater pH and thus CO_2 concentrations on million-year timescales using foraminiferal $\delta^{11}B$ values, we must take some steps that include: (1) correcting for any vital effects in extinct species; (2) constraining the $\delta^{11}B_{sw}$, which, given the 10–20 Myr ago residence time for boron in the ocean is probably different from the modern value (39.61‰)[58,59]; and (3) estimating a second carbonate system parameter to infer aqueous CO_2 concentration ($[CO_2]_{aq}$) from pH. Other necessary steps include (4) reconstructing the calcification temperature and relative habitat depth of foraminifera; (5) knowing the CO_2 disequilibrium between surface waters and atmosphere at the study site; and (6) ensuring that primary $\delta^{11}B$ values are not altered by diagenesis (mitigated here by using 'glassy' foraminifera).

Vital-effects corrections associated with the boron isotope proxy

Offsets between the boron isotopic composition of ambient seawater borate ion ($\delta^{11}B_{borate}$) and that of foraminiferal calcite ($\delta^{11}B_c$) are known as vital effects. Such vital effects develop in response to respiration, calcification and photosynthesis generating a pH gradient within the micro-environment (the diffusive boundary layer) around foraminifera[60,61]. For extant species these effects can be accounted for using species-specific $\delta^{11}B$–pH calibrations (for example, refs 9, 62–64). However, all Eocene foraminifera species are extinct and thus vital effects can only be assessed indirectly. To supplement our existing understanding of modern vital effects[22,26,62,64,65] we generated core-top (Holocene) planktonic foraminiferal $\delta^{11}B$, $\delta^{18}O$ and $\delta^{13}C$ values (Extended Data Fig. 7c and Supplementary Table 1) from offshore Tanzania (Glow 15, ref. 66). Modern foraminifera from offshore Tanzania show a substantially less coherent relationship with $\delta^{18}O$ than our Eocene samples (Extended Data Fig. 7 and Fig. 2). This increased spread is at least partly due to the known large vital effects of modern foraminifera, where offsets of 0–4‰ are required for the $\delta^{11}B$ of our modern species to match the $\delta^{11}B$ of seawater borate (Extended Data Fig. 7c).

If we apply published modern symbiont-bearing planktonic foraminifera $\delta^{11}B$–pH calibrations[22,62,64] for the shallower Eocene species, and symbiont-barren $\delta^{11}B$–pH calibrations of modern planktonic foraminifera[26,65] for the Eocene deep dwellers, an unrealistic picture emerges (Extended Data Fig. 8). Specifically, there is increased scatter between the shallowest and deepest planktonic foraminifera and inversion in pH gradients with depth. Additionally, there is clear disagreement between

Cibicidoides, that we know exhibits minimal vital effect for $\delta^{18}O$, $\delta^{11}B$ and $\delta^{13}C$ (refs 40, 67), and deeper planktonic foraminifera of similar depth (Extended Data Fig. 8), which are otherwise overlapping in $\delta^{11}B_c$ (for the 53.2-Myr-ago time slice, *S. roesnaesensis* $\delta^{11}B = 12.96 \pm 0.38$ ‰ is in agreement with *Cibicidoides*, which average 13.15 ± 0.53‰, and for the 40.3-Myr-ago time slice, the average *Subbotina* $\delta^{11}B = 12.63 \pm 0.38$‰ is within uncertainty of the *Cibicidoides* $\delta^{11}B = 12.71 \pm 0.30$‰). This suggests that modern vital effects are probably not applicable to Eocene planktonic foraminifera. Given that modern vital effects appear to be unsuitable for the Eocene, as explained above, we argue by extension that the reduced scatter in the Eocene, and notably the agreement in $\delta^{11}B_c$ among the mixed-layer species targeted in the Eocene (in stark contrast with modern values; Extended Data Fig. 7c), suggests a more minor role for vital effects in determining $\delta^{11}B$, and therefore that the targeted Eocene foraminifera must more closely reflect the $\delta^{11}B$ of ambient borate ion. Furthermore, different size fractions of the Eocene foraminifera belonging to the genus *Acarinina* from this study (Supplementary Table 1), and for Early Eocene/Palaeocene *Morozovella velascoensis* and *A. soldadoensis* in ref. 68 have $\delta^{11}B_c$ compositions within analytical uncertainty. This contrasts with the modern symbiont-bearing planktonic foraminifera *T. sacculifer* and *Globigerinoides ruber* that exhibit large changes in $\delta^{11}B$ with size (1‰ to 2.3‰; refs 64, 69), again supporting our assertion that vital effects are reduced in the Eocene foraminifera.

Although we do not yet have a full mechanistic understanding of the causes of $\delta^{11}B$ vital effects in planktonic foraminifera, a reduction in vital effects for the Eocene foraminifera would most probably result from a reduction in the relative magnitude of one or more of the following physiological processes: calcification, photosynthesis or respiration. For instance, for smaller modern foraminifera the magnitude of the influence of symbiont photosynthesis on the pH of the diffusive boundary layer is reduced, with smaller-size-fraction foraminifera recording $\delta^{11}B_c$ closer to that of seawater borate[64,69]. Here, the size of our shallower Eocene foraminifera is mostly within 212–250 μm, which is reduced compared to the modern foraminifera analysed here (300–355 μm) and elsewhere (≥425 μm; ref. 70). Also, vital-effect offsets are pH-dependent (see Extended Data Fig. 9) for symbiont-bearing foraminifera[62–64,71]. Eocene symbiotic planktonic foraminiferal composition is 15.5–14.5‰, and for this

range the *T. sacculifer* (300–355 μm; ref. 22) calibration has a minimal effect on pH estimates, as it requires only a 0.1–0.3‰ correction on $\delta^{11}B_c$ for deriving $\delta^{11}B_{borate.}$

Importantly, while the modern symbiont-bearing foraminifera calibrated to date have $\delta^{11}B$ composition offset from the seawater borate curve, only $\delta^{11}B$–pH calibrations for three dinoflagellate hosting species have so far been published[9,62–64]. Our new depth profile for the modern Indian Ocean shown in Extended Data Fig. 7c shows that some extant species (*Globigerinella siphonifera* and *Globorotalia menardii*) have minimal $\delta^{11}B_c$ offsets from seawater borate $\delta^{11}B$.

Additional support for minimal vital effects in Eocene foraminifera is also given by the relative agreement with independently calculated Eocene CO_2[5,11,19] when the borate $\delta^{11}B$–pH calibration is used (Extended Data Fig. 4). Nonetheless, we also apply the modern *T. sacculifer* calibration, because this provides an upper limit on the likely extent of $\delta^{11}B$ vital effects in Eocene foraminifera. Notably, our calculated pH and CO_2 estimates for both approaches are largely within uncertainty (Extended Data Fig. 4), highlighting that such assumptions have little influence on the conclusions drawn (Fig. 4 and Extended Data Fig. 5).

Constraints on $\delta^{11}B_{sw}$

Geochemical box models[58] and existing records of benthic foraminiferal $\delta^{11}B_c$, coupled with assumptions regarding deep-water pH evolution[72], indicate that $\delta^{11}B_{sw}$ is unlikely to have changed from its modern value by more than 2.5‰ since the EECO (with a likely maximum rate of change of 0.1‰ per million years)[58]. Here, we use new, empirically constrained, upper and lower bounds on Eocene $\delta^{11}B_{sw}$ from several independent approaches. The underlying methodology for quantifying a maximum and minimum $\delta^{11}B_{sw}$ is based on the observation that the $\delta^{11}B$ versus pH is nonlinear (Extended Data Fig. 2), and its curvature is affected by $\delta^{11}B_{sw}$; when $\delta^{11}B_{sw}$ is higher, for any given $\delta^{11}B_c$ gradient the reconstructed pH change is larger than when $\delta^{11}B_{sw}$ is lower. Furthermore, the curvature in the $\delta^{11}B$–pH relationship results in there being a pH below which the $\delta^{11}B$ system becomes unresponsive. The lowest foraminiferal $\delta^{11}B_c$ recorded in this study therefore provides the first constraint on the $\delta^{11}B_{sw}$, which then places an additional upper bound on $\delta^{11}B_{sw}$. The lowest $\delta^{11}B_c$ values we recovered are for *Subbotina crociapertura* of 11.54 ± 0.29‰ at 45.6 Myr ago, and *S.*

eocaena of 11.97 ± 0.22‰ at 40.3 Myr ago. If $\delta^{11}B_{sw} \geq 39.5$‰, these samples do not give a valid mathematical solution for the $\delta^{11}B$ versus pH relationship, so Eocene $\delta^{11}B_{sw}$ must be lower than the modern (39.6‰; ref. 59).

The lower bound for $\delta^{11}B_{sw}$ is constrained using the modern pH gradient (corrected for anthropogenic dissolved inorganic carbon) within the top ~300 m of the water column in the tropics and assuming that this represents the probable minimum pH gradient in Eocene. This assumption is justified by (1) a positive linear relationship between $\delta^{13}C$ and pH in modern[22] and Eocene seawater (Extended Data Fig. 10 based on cGENIE output[73]), and (2) larger $\delta^{13}C$ gradients between surface and deep-dwelling Eocene planktonic foraminifera than in the modern because of enhanced metabolic rates due to warmer ocean temperatures[25]. As a result, Eocene pH gradients were most probably larger than the modern equivalent and therefore our approach is conservative. Modern tropics, in non-upwelling regions, have an average pH gradient of the first 300 m equal to 0.17 (ref. 74) with an anthropogenic CO_2 correction resulting in an uncertainty of 0.003 pH units (GLODAP v1.1: Ref. 75). The 53.2-Myr-ago timeslice is used for this treatment because it has full upper-water-column depth coverage and the smallest $\delta^{11}B_c$ gradient (hence it will provide the smallest pH difference and thus the minimum $\delta^{11}B_{sw}$ value). A Monte Carlo propagation of uncertainties in pH, temperature, and composition of seawater results in the pH difference (assuming $\delta^{11}B_c = \delta^{11}B_{borate}$) between the shallowest and the deepest planktonic dwellers (ΔpH) at 53.2 Myr ago falling below 0.17 (the modern equivalent) when $\delta^{11}B_{sw} < 38.2$‰ (with 86% of simulations resulting in ≥ 0.17 ΔpH). Therefore the minimum $\delta^{11}B_{sw}$ is calculated at 38.2‰ for the whole Eocene. This exercise was repeated using the alternative methodology for dealing with $\delta^{11}B$ vital effects (assuming $\delta^{11}B_c = \delta^{11}B_{borate}$ for the deeper-dwelling non-symbiotic foraminifera, which have $\delta^{11}B_c$ within error of co-occurring *Cibicicoides*, and assuming that the shallowest foraminifera has the $\delta^{11}B$–pH calibration of modern *T. sacculifer*). The minimum constraint from 86% of potential Monte Carlo solutions is then 38.6‰.

To further constrain the maximum Eocene $\delta^{11}B_{sw}$ we used restrictions offered by estimates of Apparent Oxygen Utilization (AOU), adapted from previous approaches[7]. AOU describes the amount of dissolved oxygen consumed by the

remineralization of sinking organic carbon between a selected depth and saturated surface waters. The surface seawater oxygen concentration—that is, $[O_{2\text{-sw}}]_{sat}$—depends on SST as a result of Henry's law. Here, $\delta^{18}O$-derived SSTs are ~30–33 °C (Supplementary Table 1), so corresponding $[O_{2\text{-sw}}]_{sat}$ values are ~191–182 μmol kg^{-1} (ref. 76), with potential mean oversaturation of ~13 mmol kg^{-1} (low-latitude maximum: 0.2–0.4 ml per litre[77,78]). To calculate the upper estimate of $\delta^{11}B_{sw}$, the minimum SST of the Eocene time slices is selected, and thus the maximum $[O_{2\text{-sw}}]_{sat}$ is calculated to be 204 μmol kg^{-1}. Additionally, we assume Eocene planktonic foraminifera have an oxygen minimum tolerance threshold of 44.7 μmol kg^{-1}, analogous to the low-oxygen-accustomed *Hastigerinella digitata*[79] in the modern Monterey Bay (California). Therefore, we assume Eocene deeper-dwelling planktonic foraminifera were bathed in waters with oxygen concentrations equal to or higher than the minimum oxygen level of *H. digitata* (AOU = 204 μmol kg^{-1} minus 44.7 μmol kg^{-1} = 159.3 μmol kg^{-1}). To calculate AOU for each time slice studied, we modified $\delta^{11}B_{sw}$ (similarly following the Monte Carlo approach explained above) from the minimum constraint of 38.2‰ to modern seawater (39.6‰; ref. 59). We then first calculate the difference between the calculated (initially assuming that $\delta^{11}B_c = \delta^{11}B_{borate}$) dissolved inorganic carbon at the depth occupied by our deepest-dwelling foraminifera (average), and compare this to the dissolved inorganic carbon of the shallower-dwelling (within ~50 m of the surface on average) planktonic foraminifera. The difference in dissolved inorganic carbon is then transformed into AOU using Redfield ratios (106:138, CO_2:O_2). The AOU is ≤159.3 μmol kg^{-1} when $\delta^{11}B_{sw}$ is at maximum 38.5‰ for the 45.6-Myr-ago time slice and 38.7‰ for the 40.3-Myr-ago time slice, resulting in 86% of potential solutions with our Monte Carlo approach satisfying the AOU constraint. The same approach was used applying the *T. sacculifer* calibration for the shallowest planktonic foraminifera, resulting in a maximum $\delta^{11}B_{sw}$ of 38.8‰ and 38.9‰ for the 45.6-Myr-ago and 40.3-Myr-ago time slice respectively. To be conservative, we use the maximum of the two estimates for each calibration method. In summary, although we are calculating the lower $\delta^{11}B_{sw}$ bound at 53.2 Myr ago and the upper at 40.3 and 45.6 Myr ago, we apply this range across the whole of the study interval (53.2–36.9 Myr ago).

Second carbonate parameter

After calculating seawater pH using $\delta^{11}B_{sw}$ and $\delta^{11}B_c$, an additional carbonate parameter is required to calculate CO_2 concentrations at any given seawater salinity and temperature. Here the second parameter we use is the saturation state of calcium carbonate (surface $\Omega_{calc} = [CO_3^{2-}]/[CO_3^{2-}]_{saturation}$). Typically, for the pre-industrial tropical surface ocean Ω_{calc} is ~6, while for Eocene Tanzania waters it is ~7 (ref. 27; Extended Data Fig. 3). In support of the narrow range of potential Ω_{calc}, a variety of modelling studies of the early Cenozoic show that surface water Ω_{calc} remains within ±1, essentially constant in the early Cenozoic, independent of model boundary conditions[23,80–82]. Therefore, here we assume surface Ω_{calc} was equal to 6.5 ± 1 throughout the Eocene.

Monte Carlo pH–CO₂ estimates from planktonic foraminiferal $\delta^{11}B_c$

Atmospheric CO_2 was calculated using a Monte Carlo approach to solving the relevant carbonate system equations with 10,000 iterations, deriving mean, upper and lower bounds of 95% of the simulations. We use the following constraints for our calculations: average seawater composition for $[Ca]_{sw} = 17$ mmol kg^{-1} (refs 83–87), $[Mg]_{sw} = 38 \pm 3$ mmol kg^{-1} (ref. 84) (see also Supplementary Table 2), salinity 35 ± 2, and temperature ± 2°C (with temperature derived from $\delta^{18}O$ of the shallowest-dwelling species). All simulations are iterated assuming Gaussian distribution of these parameters within the stated 2 s.d. A similar distribution is also applied to the $\delta^{11}B_c$ of the warmest and thus shallowest-dwelling species for each timeslice (Supplementary Table 2). We did not have sufficient shallow dwellers in the 36.9-Myr-ago time slice for boron isotope work. Thus, the intermediate dweller *Turborotalia cerroazulensis* was used. *T. cerroazulensis* was also analysed in the 40.3-Myr-ago time slice, and its $\delta^{11}B_c$ and $\delta^{18}O$ offset (and uncertainty) from *Morozovelloides lehneri*, (the shallowest dweller in the same timeslice) was applied to estimate the shallowest temperature at 36.9 Myr ago (Supplementary Table 2). The temperature offsets between species beyond the ±2 °C uncertainty applied to our calculations are considered unlikely. Note that a Gaussian distribution is not applicable to $\delta^{11}B_{sw}$ because there is equal likelihood that it falls between the minimum and maximum constraints; we therefore applied a uniform 'flat' probability $\delta^{11}B_{sw}$ for the Monte Carlo simulations. The

relative magnitude of each component of our error propagation is shown in Extended Data Fig. 4.

Correction to pH–CO$_2$ estimates from *T. ampliapertura* $\delta^{11}B_c$

We compared $\delta^{18}O$ measurements of the surface dwellers *Planoglobanomalina* and *Pseudohastigerina* in the Eocene and early Oligocene[35,88] with that of *T. ampliapertura* used in ref. 12, and confirmed that *T. ampliapertura* gives a slightly cooler temperature than *Pseudohastigerina*. On average, when contemporaneous shallow-dwelling planktonic foraminifera are available, *T. ampliapertura* are offset by about +0.3‰ in $\delta^{18}O$ and therefore occupy a shallower water depth than *T. cerroazulensis* (whose $\delta^{18}O$ value is consistently ~0.5‰ higher than contemporaneous Eocene shallow-dwelling planktonic foraminifera). Further, considering the $\delta^{11}B$ offset between *T. cerroazulensis* and the shallow-dwelling *M. lehneri* in the 40.3-Myr-ago time slice, we apply a +1‰ correction to *T. ampliapertura* $\delta^{11}B$ values of ref. 12 to estimate surface seawater values.

Climate sensitivity calculations

Our new CO$_2$ reconstructions allow us to examine their role in driving long-term Eocene cooling. Climate forcing compared to the early Eocene timeslice at 53.2 Myr ago is calculated from equation (1)[28] for our two CO$_2$ scenarios. We then assume that the apparent latitudinal SST sensitivity for the Eocene was similar to that of the last ~520 kyr (ref. 13). Estimates of SST change per W m^{-2} forcing for each degree of latitude were generated using the second-order polynomial fit through the data of ref. 13 (dotted line in Fig. 4b, Extended Data Fig. 5b). As a high-latitude SST sensitivity we used the average of estimates for 60° N and 60° S (1.63 K per W m^{-2}); as a low-latitude estimate we used the average of values between 30° S and 30° N (0.36 K per W m^{-2}). We use the ratio of high- or low-latitude SST sensitivity and forcing for each timeslice to calculate the SST change expected as a result of our reconstructed CO$_2$ forcing. The product gives the estimated SST change of Fig. 4c and Extended Data Fig. 5c for high (blue symbols) and low (red symbols) latitudes driven by CO$_2$. The uncertainties (Fig. 4c, Extended Data Fig. 5c) are the product of 1,000 realizations of each CO$_2$ estimate within its uncertainty envelope (95% confidence intervals).

To test the importance of CO$_2$ to early and late Eocene warmth, we calculated the sensitivity of the Earth system to radiative forcing, the ECS. For ΔT we use global

mean surface temperature for the EECO and late Eocene, where the EECO ΔT is thought to be ~14 ± 3 °C warmer than the pre-industrial global mean surface temperature, and ~5 °C warmer than the late Eocene global mean surface temperature (35 Myr ago)[2,29]. Of this ΔT, 4–6 °C is attributed to changes in boundary conditions (palaeotopography and continental configuration of the Eocene) and the action of the slow climate feedbacks (mainly the lack of a continental ice sheet on Antarctica and vegetation change[2–4]), for both the early and late Eocene. The uncertainties in Fig. 4d to 4f (and Extended Data Fig. 5d–f) are the products of 1,000 realizations of the 53.2-Myr-ago and 36.9-Myr-ago CO_2 values and the ΔT estimate based on randomly sampling each variable within its 95% confidence interval uncertainty envelope. The uncertainty for the CO_2 and ΔT estimates follows a Gaussian distribution, and for the slow-feedback correction on ΔT follows a uniform 'flat' probability.

Data

The underlying data of this manuscript may be found in the Supplementary Tables 1 and 2.

31.   Nicholas, C. J. *et al.* Stratigraphy and sedimentology of the Upper Cretaceous to Paleogene Kilwa Group, southern coastal Tanzania. *J. Afr. Earth Sci.* **45,** 431–466 (2006).

32.   Pearson, P. N. *et al.* Further Paleogene and Cretaceous sediment cores from the Kilwa area of coastal Tanzania: Tanzania Drilling Project Sites 6-10. *J. Afr. Earth Sci.* **45,** 279–317 (2006).

33.   Kent, P. E., Hunt, J. A. & Johnstone, D. W. The geology and geophysics of coastal Tanzania. Geophys. Paper No. 6, 1-101 (Her Majesty's Stationary Office, Inst. Geol. Sci, 1971).

34.   Bown, P. R. *et al.* A Paleogene calcareous microfossil Konservat-Lagerstätte from the Kilwa Group of coastal Tanzania. *Geol. Soc. Am. Bull.* **120,** 3–12 (2008).

35.   Pearson, P. N. *et al.* Stable warm tropical climate through the Eocene Epoch. *Geology* **35,** 211–214 (2007).

36.   van Dongen, B. E. *et al.* Well preserved Palaeogene and Cretaceous biomarkers from the Kilwa area, Tanzania. *Org. Geochem.* **37,** 539–557 (2006).

37.   Takahashi, T. *et al.* Climatological mean and decadal change in surface ocean pCO_2, and net sea-air CO_2 flux over the global oceans. *Deep Sea Res. II* **56,** 554–577 (2009).

38.   Barker, S., Greaves, M. & Elderfield, H. A study of cleaning procedures used for foraminiferal Mg/Ca paleothermometry. *Geochem. Geophys. Geosyst.* **4,** 8407 (2003).

39.   Yu, J., Elderfield, H., Greaves, M. & Day, J. Preferential dissolution of benthic foraminiferal calcite during laboratory reductive cleaning. *Geochem. Geophys. Geosys.* **8,** Q06016 (2007).

40.   Rae, J. W. B., Foster, G. L., Schmidt, D. N. & Elliott, T. Boron isotopes and B/Ca in benthic foraminifera: proxies for the deep ocean carbonate system. *Earth Planet. Sci. Lett.* **302,** 403–413 (2011).

41.   Edgar, K. M., Anagnostou, E., Pearson, P. N. & Foster, G. L. Assessing the impact of diagenesis on $d^{11}B$, $d^{13}C$, $d^{18}O$, Sr/Ca and B/Ca values in fossil planktic foraminiferal calcite. *Geochim. Cosmochim. Acta* **166,** 189–209 (2015).

42.   Kim, S.-T. & O'Neil, J. R. Equilibrium and non-equilibrium oxygen isotope effects in synthetic carbonates. *Geochim. Cosmochim. Acta* **61,** 3461–3475 (1997).

43.   Cramer, B. S., Miller, K. G., Barrett, P. J. & Wright, J. D. Late Cretaceous–Neogene trends in deep ocean temperature and continental ice volume: reconciling records of benthic foraminiferal geochemistry ($d^{18}O$ and Mg/Ca) with sea level history. *J. Geophys. Res.* **116,** C12023 (2011).

44.   Zachos, J. C., Stott, L. D. & Lohmann, K. C. Evolution of early Cenozoic marine temperatures. *Paleoceanography* **9,** 353–387 (1994).

45.   Pearson, P. N. in *Reconstructing Earth's Deep Time Climate—The State of the Art in 2012* Vol. 18 (eds Ivany, L. C. & Huber, B. T.) 1–38 (The Paleontological Society, 2012).

46. LeGrande, A. N. & Schmidt, G. A. Global gridded data set of the oxygen isotopic composition in seawater. *Geophys. Res. Lett.* **33,** L12604 (2006).

47. Sexton, P. F., Wilson, P. A. & Pearson, P. N. Palaeoecology of late middle Eocene planktic foraminifera and evolutionary implications. *Mar. Micropaleontol.* **60,** 1–16 (2006).

48. Pearson, P. N., Shackleton, N. J. & Hall, M. A. Stable isotope paleoecology of middle Eocene planktonic foraminifera and multi-species isotope stratigraphy, DSDP Site 523, South Atlantic. *J. Foraminiferal Res.* **23,** 123–140 (1993).

49. Pearson, P. N. *et al.* Warm tropical sea surface temperatures in the Late Cretaceous and Eocene epochs. *Nature* **413,** 481–487 (2001).

50. Edgar, K. M. *et al.* Symbiont 'bleaching' in planktic foraminifera during the Middle Eocene Climatic Optimum. *Geology* **41,** 15–18 (2013).

51. Birch, H. *et al.* Planktonic foraminifera stable isotopes and water column structure: disentangling ecological signals. *Mar. Micropaleontol.* **101,** 127–145 (2013).

52. Fairbanks, R. G. & Wiere, P. H. & Bé, A. W. H. Vertical distribution and isotopic composition of living planktonic foraminifera in the western North Atlantic. *Science* **207,** 61–63 (1980).

53. Spero, H. & Williams, D. F. Extracting environmental information from planktonic foraminiferal d^{13}C data. *Nature* **335,** 717–719 (1988).

54. Berger, W. H., Killingley, J. S. & Vincent, E. Stable isotopes in deep-sea carbonates: Box Core ERDC-92, West Equatorial Pacific. *Oceanol. Acta* **1,** 203–216 (1978).

55. Seki, O. *et al.* Alkenone and boron-based Pliocene pCO_2 records. *Earth Planet. Sci. Lett.* **292,** 201–211 (2010).

56. Hönisch, B. *et al.* Atmospheric carbon dioxide concentration across the Mid-Pleistocene transition. *Science* **324,** 1551–1554 (2009).

57. Sanyal, A. & Bijma, J. A comparative study of the northwest Africa and eastern equatorial Pacific upwelling zones as sources of CO_2 during glacial

periods based on boron isotope paleo-pH estimation. *Paleoceanography* **14,** 753–759 (1999).

58.   Lemarchand, D., Gaillardet, J., Lewin, E. & Allegre, C. J. The influence of rivers on marine boron isotopes and implications for reconstructing past ocean pH. *Nature* **408,** 951–954 (2000).

59.   Foster, G. L., Pogge von Strandmann, P. A. E. & Rae, J. W. B. Boron and magnesium isotopic composition of seawater. *Geochem. Geophys. Geosyst.* **11,** Q08015 (2010).

60.   Rink, S., Kühl, M., Bijma, J. & Spero, H. J. Microsensor studies of photosynthesis and respiration in the symbiotic foraminifer *Orbulina universa. Mar. Biol.* **131,** 583–595 (1998).

61.   Zeebe, R. E., Wolf-Gladrow, D. A., Bijma, J. & Hönisch, B. Vital effects in foraminifera do not compromise the use of $d^{11}B$ as a paleo-pH indicator: evidence from modelling. *Paleoceanography* **18,** 1043 (2003).

62.   Sanyal, A. *et al.* Oceanic pH control on the boron isotopic composition of foraminifera: evidence from culture experiments. *Paleoceanography* **11,** 513–517 (1996).

63.   Sanyal, A., Bijma, J., Spero, H. & Lea, D. W. Empirical relationship between pH and the boron isotopic composition of *Globigerinoides sacculifer*: implications for the boron isotope paleo-pH proxy. *Paleoceanography* **16,** 515–519 (2001).

64.   Henehan, M. J. *et al.* Calibration of the boron isotope proxy in the planktonic foraminifera *Globigerinoides ruber* for use in palaeo-CO_2 reconstruction. *Earth Planet. Sci. Lett.* **364,** 111–122 (2013).

65.   Yu, J., Thornalley, D. J. R., Rae, J. W. B. & McCave, N. I. Calibration and application of B/Ca, Cd/Ca, and $d^{11}B$ in *Neogloboquadrina pachyderma* (sinistral) to constrain CO_2 uptake in the subpolar North Atlantic during the last deglaciation. *Paleoceanography* **28,** 237–252 (2013).

66.   Kroon, D. & the Shipboard Scientific Party. Tropical temperature history during Paleogene Global Warming (GLOW) events. NIOZ: Netherlands

Institute for Sea Research, Site Survey Cruise Report (RV *Pelagia* cruise number 64PE303) 1–151 (2010).

67. McCorkle, D., Corliss, B. & Farnham, C. Vertical distributions and stable isotopic compositions of live (stained) benthic foraminifera from the North Carolina and California continental margins. *Deep Sea Res. I* **44,** 983–1024 (1997).

68. Penman, D. E. *et al.* Rapid and sustained surface ocean acidification during the Paleocene-Eocene Thermal Maximum. *Paleoceanography* **29,** 2014PA002621 (2014).

69. Hönisch, B. & Hemming, N. G. Ground-truthing the boron isotope-paleo-pH proxy in planktonic foraminifera shells: partial dissolution and shell size effects. *Paleoceanography* **19,** PA4010 (2004).

70. Martínez-Botí, M. A. *et al.* Boron isotope evidence for oceanic carbon dioxide leakage during the last deglaciation. *Nature* **518,** 219–222 (2015).

71. Hönisch, B. *et al.* The influence of symbiont photosynthesis on the boron isotopic composition of foraminifera shells. *Mar. Micropaleontol.* **49,** 87–96 (2003).

72. Raitzsch, M. & Hönisch, B. Cenozoic boron isotope variations in benthic foraminifers. *Geology* **41,** 591–594 (2013).

73. John, E. H., Wilson, D. J., Ridgwell, A. & Pearson, P. N. Temperature-dependent remineralization and carbon cycling in the warm Eocene oceans. *Palaeogeogr. Palaeoclimatol. Palaeoecol.* **413,** 158–166 (2014).

74. Goyet, C., Healy, R. J. & Ryan, J. P. Global distribution of total inorganic carbon and total alkalinity below the deepest winter mixed layer depths. Report ORNL/CDIAC-127, NDP-076 (Carbon Dioxide Information Analysis Center, Oak Ridge National Laboratory, US Department of Energy, 2000).

75. Key, R.M. *et al.* A global ocean carbon climatology: Results from the Global Data Analysis Project (GLODAP). *Glob. Biogeochem. Cycles* **18**, GB 4031, (2004).

76. Battino, R., Rettich, T. R. & Tominaga, T. The solubility of oxygen and ozone in liquids. *J. Phys. Chem. Ref. Data* **12,** 163–178 (1983).

77. Jenkins, W. J. & Goldman, J. C. Seasonal oxygen cycling and primary production in the Sargasso Sea. *J. Mar. Res.* **43,** 465–491 (1985).

78. Sarmiento, J. L. & Gruber, N. *Ocean Biogeochemical Dynamics*. 1-528 (Princeton Univ. Press, 2006).

79. Hull, P. M., Osborn, K. J., Norris, R. D. & Robinson, B. H. Seasonality and depth distribution of a mesopelagic foraminifer, *Hastigerinella digitata*, in Monterey Bay, California. *Limnol. Oceanogr.* **56,** 562–576 (2011).

80. Pälike, H. *et al.* A Cenozoic record of the equatorial Pacific carbonate compensation depth. *Nature* **488,** 609–614 (2012).

81. Ridgwell, A. & Zeebe, R. E. The role of the global carbonate cycle in the regulation and evolution of the Earth system. *Earth Planet. Sci. Lett.* **234,** 299–315 (2005).

82. Tyrrell, T. & Zeebe, R. E. History of carbonate ion concentration over the last 100 million years. *Geochim. Cosmochim. Acta* **68,** 3521–3530 (2004).

83. Coggon, R. M. *et al.* Reconstructing past seawater Mg/Ca and Sr/Ca from mid-ocean ridge flank calcium carbonate veins. *Science* **327,** 1114–1117 (2010).

84. Horita, J., Zimmermann, H. & Holland, H. D. Chemical evolution of seawater during the Phanerozoic: implications for the record of marine evaporites. *Geochim. Cosmochim. Acta* **66,** 3733–3756 (2002).

85. Dickson, A. J. Fossil echinoderms as monitor of the Mg/Ca ratio of Phanerozoic oceans. *Science* **298,** 1222–1224 (2002).

86. Lowenstein, T. K. *et al.* Oscillations in the Phanerozoic seawater chemistry: evidence from fluid inclusions. *Science* **294,** 1086–1088 (2001).

87. Lear, C. H., Elderfield, H. & Wilson, P. A. Cenozoic deep-sea temperatures and global ice volumes from Mg/Ca in benthic foraminiferal calcite. *Science* **287,** 269–272 (2000).

88. Wade, B. S. & Pearson, P. N. Planktonic foraminiferal turnover, diversity fluctuations and geochemical signals across the Eocene/Oligocene boundary in Tanzania. *Mar. Micropaleontol.* **68**, 244-255 (2008).

89.   Huber, M. & Caballero, R. The early Eocene equable climate problem revisited. *Clim. Past* **7,** 603–633 (2011).

90.   Tindall, J. *et al.* Modelling the oxygen isotope distribution of ancient seawater using a coupled ocean-atmosphere GCM: implications for reconstructing early Eocene climate. *Earth Planet. Sci. Lett.* **292,** 265–273 (2010).

91.   Wade, B. S., Pearson, P. N., Berggren, W. A. & Pälike, H. Review and revision of Cenozoic tropical planktonic foraminiferal biostratigraphy and calibration to the geomagnetic polarity and astronomical time scale. *Earth Sci. Rev.* **104,** 111–142 (2011).

92.   Ben-Yaakov, S. & Goldhaber, M. B. The influence of sea water composition on the apparent constants of the carbonate system. *Deep-Sea Res.* **20,** 87–99 (1973).

93.   Millero, F. J. & Pierrot, D. A chemical equilibrium model for natural waters. *Aquat. Geochem.* **4,** 153–199 (1998).

94.   Hershey, J. P., Fernandez, M., Milne, P. J. & Millero, F. J. The ionization of boric acid in NaCl, Na-Ca-Cl and Na-Mg-Cl solutions at 25°C. *Geochim. Cosmochim. Acta* **50,** 143–148 (1986).
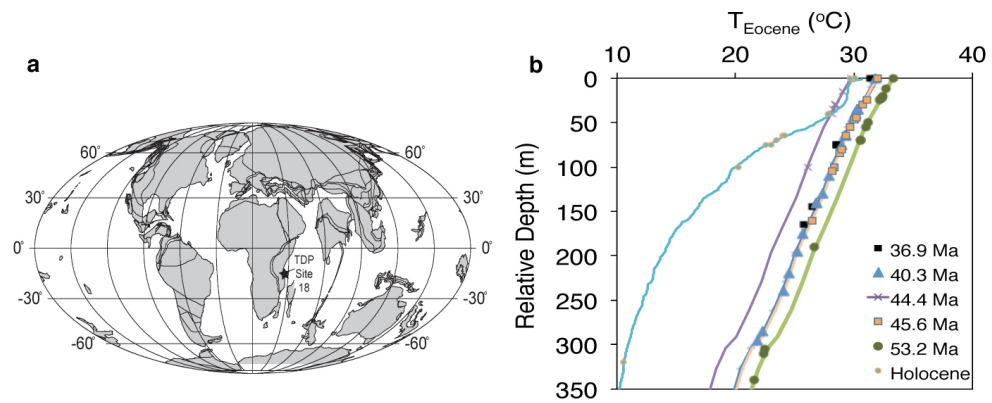
Extended Data Fig. 1 Palaeogeography and δ^{18}O-derived temperature against foraminiferal calcification depth. a, Approximate palaeoposition of Tanzanian Drilling Project (TDP) sites studied here (map generated from www.odsn.de). **b**, Reconstructed temperature (T$_{Eocene}$) and relative depth of each foraminifera within each time slice. The pale blue line represents the output of a General Circulation Model simulation run with Eocene boundary conditions[89,90], whereas the other coloured lines show the General Circulation Model output offset to intersect with the warmest temperature at depth zero for each time slice. Note that depth assignments are approximate (see Methods). Also shown are the reconstructed temperatures from Holocene planktonic foraminiferal δ^{18}O (Supplementary Table 1), where *G. ruber* is assigned a depth of zero and the rest of the planktonic foraminifera are offset to reproduce the measured temperature profile at GLOW15[51,66]. For Holocene temperature reconstructions we used the modern site latitude of 9° S, and δ^{18}O$_{sw}$ (using the Standard Mean Ocean Water (SMOW) standard) of 0‰.
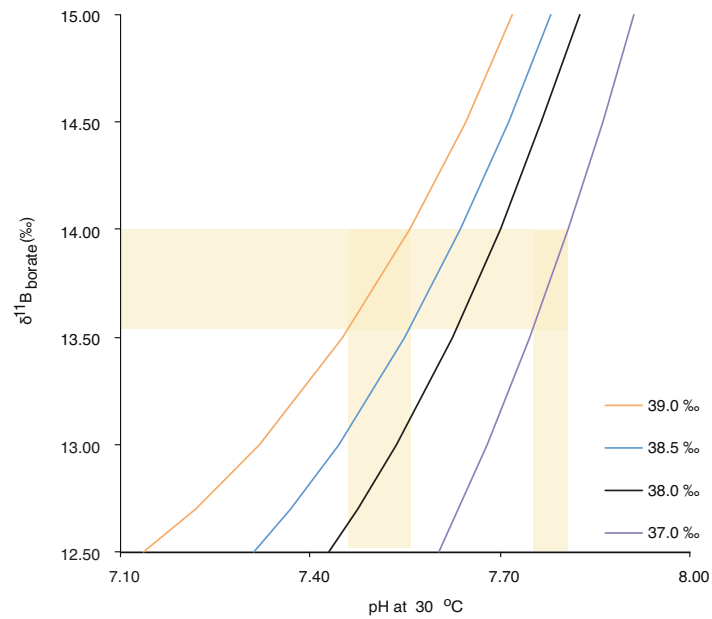
**Extended Data Fig. 2 δ^{11}B versus pH as a function of δ^{11}B$_{sw}$.** Increasing δ^{11}B$_{sw}$, as indicated in the legend, results in lower pH for the same δ^{11}B. However, for the same δ^{11}B range, the reconstructed pH range is larger for higher δ^{11}B$_{sw}$ (see brown-shaded regions).
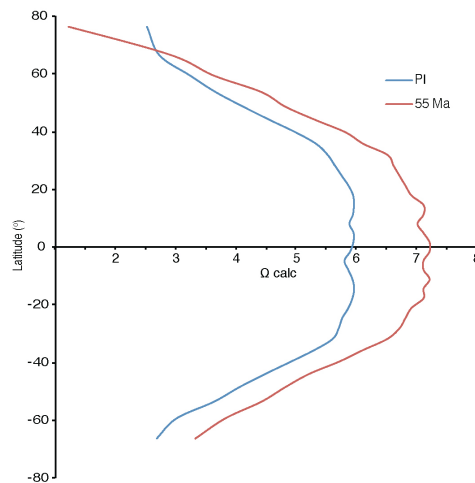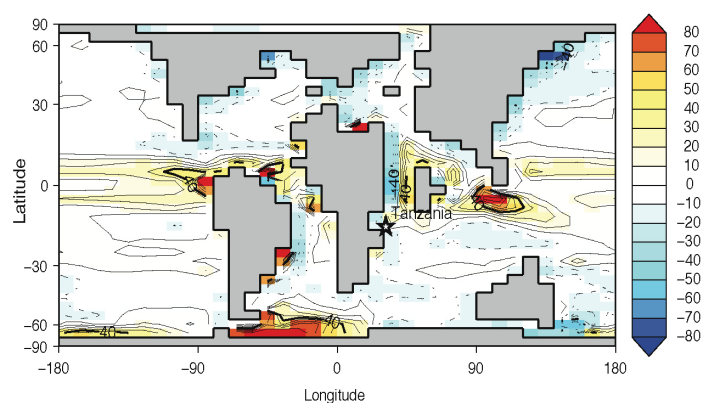

Extended Data Fig. 3 cGENIE estimates of calcite saturation in surface waters. Comparison of calcite saturation Ω_{calc} for pre-industrial times (PI; blue) and 55 Myr ago (red) at different latitudes.
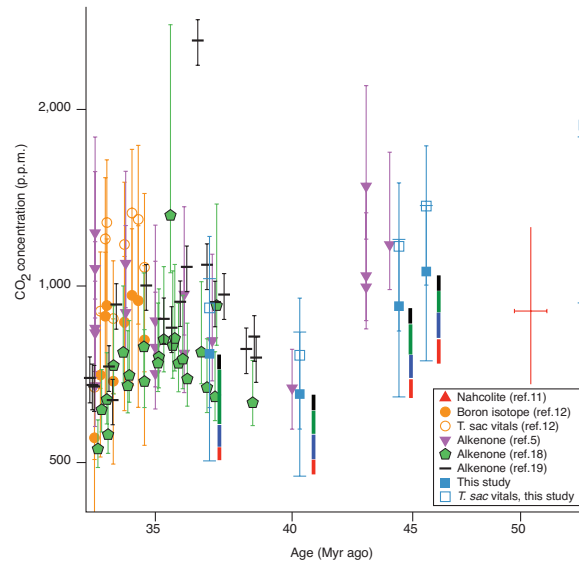
Extended Data Fig. 4 Compilation of several CO$_2$ records for the Eocene in comparison to this study. Data are from refs 5, 11, 12, 18 and 19. The contribution of different parameters to the uncertainty on our CO$_2$ reconstructions is colour-coded; sequentially from bottom to top, red is from $\delta^{11}B_{sw}$, blue is from the Ω_{calc} uncertainty, green is from the $\delta^{11}B_c$ error, black is the 40 p.p.m. uncertainty in the event of disequilibrium with the atmosphere. Other parameters contribute <10% uncertainty to the CO$_2$ calculations and are not shown. Note that the data from Pearson *et al.*[12] (orange circles) are corrected as in Fig. 3, and there are two scenarios included for the Tanzania records of ref. 12 and this study: one with $\delta^{11}B_c = \delta^{11}B_{borate}$ (closed blue and orange symbols) and the other applying *T. sacculifer* (open blue and orange symbols) corrections to the shallowest symbiotic planktonic foraminifera (Methods). The y axis is in log-scale. Error bars are representative of each proxy's reconstruction uncertainty (typically at 95% confidence). For the $\delta^{11}B$ reconstructions in this study, the errors are based on Monte Carlo propagation of relevant errors (Methods).
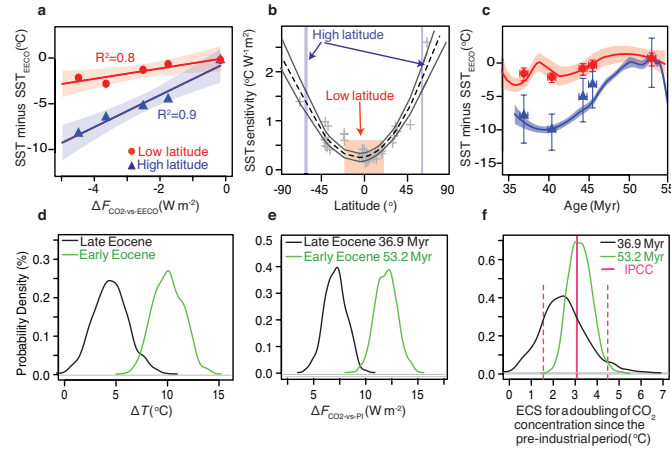
Extended Data Fig. 5 CO$_2$ as a driver of latitudinal cooling in the Eocene, and ECS analyses of the EECO and late Eocene time slices. The case for the *T. sacculifer* calibration applied to shallowest planktonic foraminifera. **a**, Evolving relationship between SST[14] for high (blue) and low (red) latitudes and the CO$_2$ forcing of each of our time slices relative to the EECO. Linear regression fits and coefficients of determination (R^2) are also shown, with the 95% confidence interval (shaded bands). **b**, Apparent latitudinal SST sensitivity for the last 520 kyr (ref. 13). The dashed line is a second-order polynomial through the SST sensitivity data (grey crosses) of ref. 13, and the grey lines show the 95% confidence interval. A red rectangle surrounds the SST sensitivity estimates averaged as a low-latitude mean, and the blue line indicates the high-latitude mean (see text and Methods). **c**, Reconstructed (lines) and estimated (symbols) SST relative to 53.2 Myr ago. Symbols show each of our time slices, calculated using the respective CO$_2$ reconstructions and the average low- (red) and high- (blue) latitude SST sensitivities of **b**. Bold lines and shaded uncertainty band (at 95% confidence) show the reconstructed long-term mean SST estimates using the TEX$_{86}$ proxy at high (blue colour >55°) and low (red colour <30°) latitudes[14] relative to the SST ~53 Myr ago. Error bars represent full propagation of errors at 95% confidence[14]. **d**, Range in mean surface temperature change for early (green) and late (black) Eocene corrected for changes due to slow feedbacks[2,4,21,29]. **e**, Forcing compared to the pre-industrial period, calculated using our CO$_2$ reconstructions for the time slices 53.2 Myr ago (early Eocene) and 36.9 Myr ago (late Eocene) (see Methods). **f**, Probability density functions of ECS for the early (green) and late (black) Eocene compared to IPCC estimates (dashed lines show the 95% confidence interval (solid pink line)).

Extended Data Fig. 6 The cGENIE estimates of air–seawater CO$_2$ disequilibrium.
The colour scale shows the difference between pCO$_2$ in air and pCO$_2$ in sea water.
The model uses Eocene boundary conditions and positive values mean that seawater is
a source of CO$_2$ (in parts per million), and star shows the palaeo-location of Tanzania.
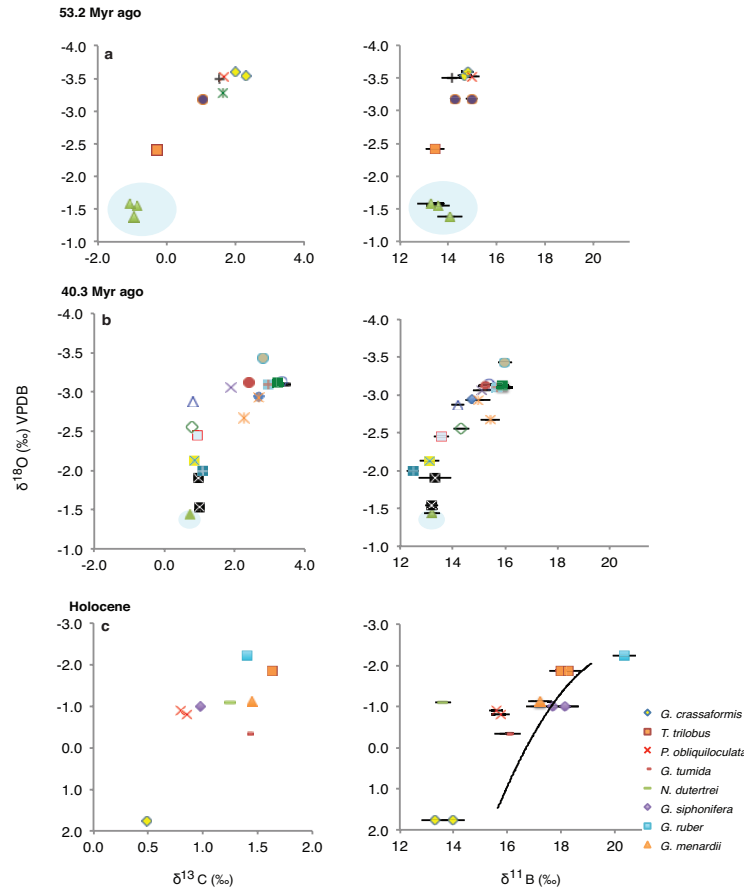
Extended Data Fig. 7 Comparison of Eocene and modern planktonic foraminiferal δ¹¹B and δ¹³C with δ¹⁸O. **a** and **b** show analyses from the time slices 53.2 Myr ago and 40.3 Myr ago, respectively (as in Fig. 2 and Supplementary Table 1). *Cibicidoides (Cibs.)* species are shaded in blue. **c**, Core-top (Holocene) offshore Tanzania foraminiferal measurements. Seawater δ¹¹B_borate and δ¹⁸O was calculated from temperature, alkalinity and dissolved inorganic carbon measurements (from GLODAP cruises 18 and 23, stations 17742 and 23037, and 53.96 °E to 7.04 °S and 52.37 °E to 6.33 °S, respectively), correcting for anthropogenic carbon input. The black line in **c** represents seawater-derived δ¹⁸O and δ¹¹B_borate data (Methods). The symbols for the time slices 53.2 and 40.3 Myr ago are as in Fig. 2. Note the change in scale for the *x* axis between the Eocene and Holocene panels. Errors in δ¹¹B represent 2 s.d. of long-term precision (Methods).
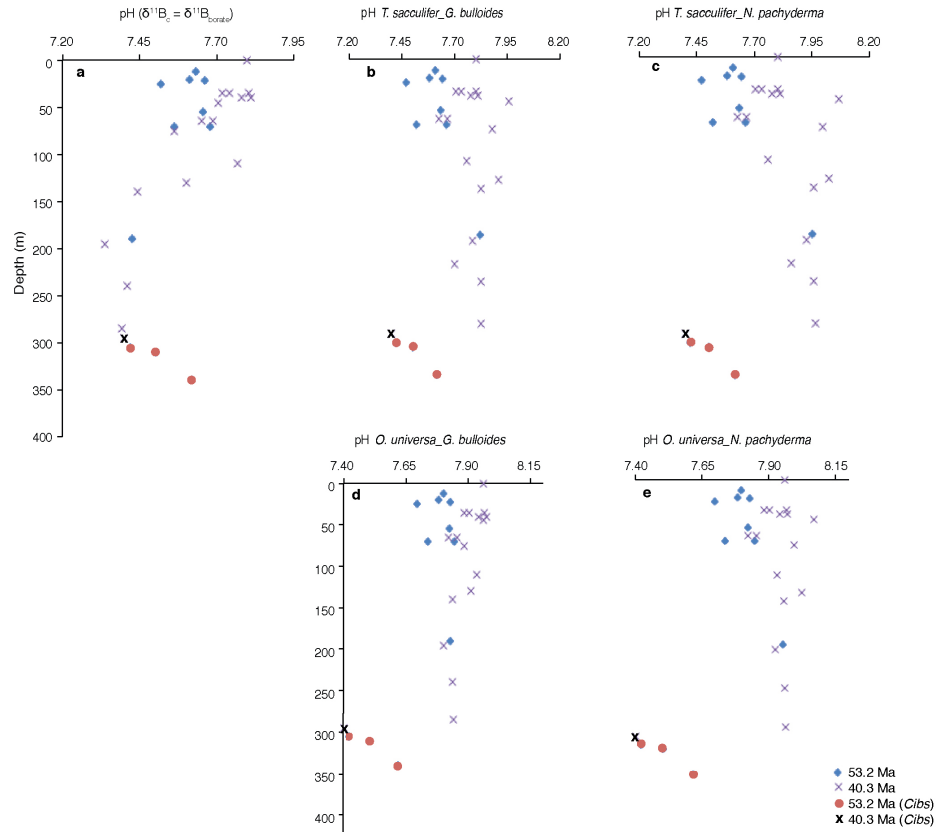
Extended Data Fig. 8 Reconstructed pH using different combinations of published symbiont-bearing and non-symbiotic foraminiferal vital-effect calibrations for the two most complete with depth time slices. a shows the case where no vital effect corrections were applied for comparison. The vital-effect corrections for deeper asymbiotic planktonic foraminifera are based on either *Globigerina bulloides*[26] (**b** and **d**) and *Neogloboquadrina pachyderma*[65] (**c** and **e**) calibrations. For shallow symbiont bearing planktonics we used calibrations specific to modern shallow, symbiont-bearing *Trilobatus sacculifer*[22] (**b** and **c**) and *Orbulina universa*[62] (**d** and **e**) (as recalculated by ref. 64 and offset by −3‰ to account for analytical differences between negative thermal ionization mass spectrometry and MC-ICPMS instrumentation[8,9]). For comparison we also show the pH reconstructions for the case where we assume $\delta^{11}B_c = \delta^{11}B_{borate}$.
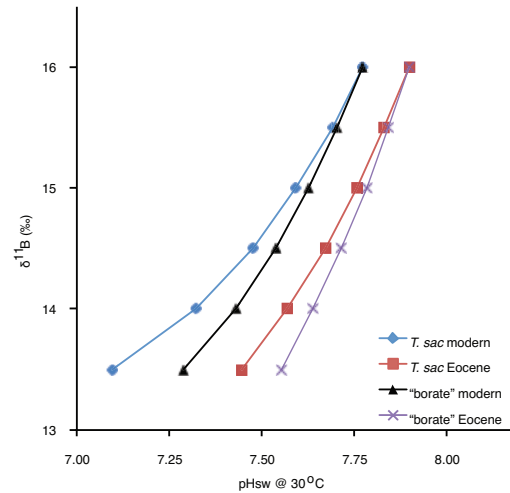
Extended Data Fig. 9 The effect of seawater composition on boron isotope calibrations in foraminifera. The example of *T. sacculifer* calibration[22] and the 'borate' calibration (assuming $\delta^{11}B_c = \delta^{11}B_{borate}$) for modern and Eocene seawater compositions; see Methods and Supplementary Table 2.
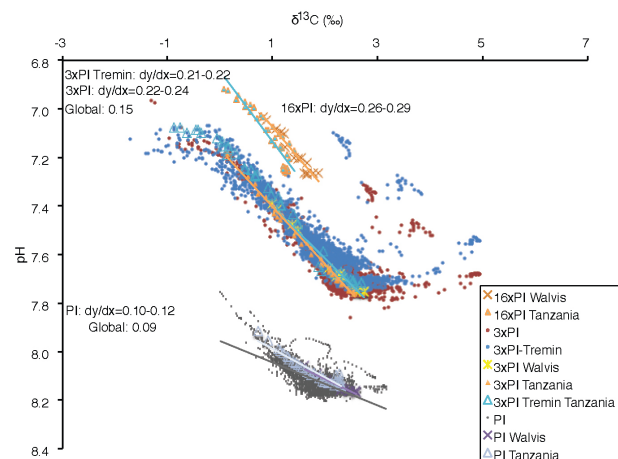
Extended Data Fig. 10 cGENIE output of seawater pH versus $\delta^{13}C$ for the top ~300 m of the ocean. The scenarios explored are from offshore Tanzania (triangles), Walvis Ridge (South Atlantic Ocean) (crosses), and the global ocean (circles) at three different atmospheric CO_2 concentrations (modern, 3× pre-industrial and 16× pre-industrial, PI). An additional scenario showing 3× pre-industrial CO_2 but considering the temperature effect on remineralization (indicated as Tremin) is also shown as blue squares and triangles.